In: EUSAR 2022: 14th European Conference on Synthetic Aperture Radar, Leipzig, 25-27 July 2022
https://ieeexplore.ieee.org/document/9944219

Polarimetric bistatic SAR image coherence

Alexander Hagelberg[a], Daniel Andre[a], Mark Finnis[b]
[a] Centre for Electronic Warfare, Information and Cyber, Cranfield University, Defence Academy of the United Kingdom, Shrivenham, UK.
[b] Centre for Defence Engineering, Cranfield University, Defence Academy of the United Kingdom, Shrivenham, UK.

Abstract

Synthetic Aperture Radar (SAR) Coherent Change Detection (CCD) allows the detection of very small scene changes, such as from ground subsidence or vehicle tracks, with applications both civilian and military. This high sensitivity to small changes can mean that differences in collection geometry or in polarisation can lead to significant changes in image coherence. This paper investigates the coherence between different bistatic SAR image geometries and their corresponding spatial frequency supports. It also investigates methods used to model coherence. The investigation employed both simulations and measured multistatic data collected at the Ground Based SAR Laboratory at Cranfield University.

1 Introduction

Synthetic Aperture Radar (SAR) allows the formation of high-resolution radar images, however without additional processing they can be hard to interpret and compare, when looking at two images from different times. Coherent Change Detection (CCD) between two SAR images, however, can highlight subtle changes between them [1]. Whilst CCD offers the potential for picking out small changes, it is reliant on a high degree of coherence between the two images.

The choice of bistatic geometry and polarimetric decomposition will affect the corresponding Radar Cross Section (RCS) values over SAR images and is thus likely to have an effect on the coherence between different bistatic SAR images [2].

This paper investigates bistatic polarimetric coherence with a view to improving CCD results for multistatic collections and is based on measured data collected with the Ground Based SAR (GBSAR) system at Cranfield University [3, 4].

Multistatic and bistatic CCD geometries are becoming an increasingly viable proposition for remote sensing of large areas of land. The cost of launching payloads to orbit has reduced to below $2000 per Kg depending on the launch vehicle [5]. This makes the possibility of large SAR satellite constellations, more feasible. It is however important to be able to understand and predict the expected coherence.

This paper begins by providing some background information and then describing the laboratory environment and methodology used in the experiment. Results, discussion, and a conclusion are then provided.

2 Background

The scattering response, or RCS, of a scatterer, changes depending on the SAR geometry bistatic angle, and the polarisation measured [2].

There are four linear polarisations HH, VV, HV and VH, from which all other polarimetric decompositions can be formed. In general, for bistatic geometries, the two cross-polarisation (HV and VH) RCS values are different.

Understanding the dependence of SAR image coherence between different bistatic geometries and how it relates to the spatial frequency domain is likely to prove beneficial in the detection of changes between multistatic SAR collections.

The SAR coherence between two images is calculate using the standard equation for CCD [6, 7, 8], giving the sample coherence, γ, which is the absolute value of a correlation between 2 images,

$$\gamma = \frac{|\sum_{k=1}^{N} S_1(k) S_2^*(k)|}{\sqrt{\sum_{k=1}^{N} |S_1(k)|^2 \sum_{k=1}^{N} |S_2(k)|^2}} \qquad (1)$$

Where S_1 and S_2 are the two complex images being compared and N is the number of pixels within a window sampled over the two images. The coherence is presented on a pixel-by-pixel basis to produce a coherence "CCD" image, and an average can be taken for the desired image area.

2.1 GBSAR laboratory measurements

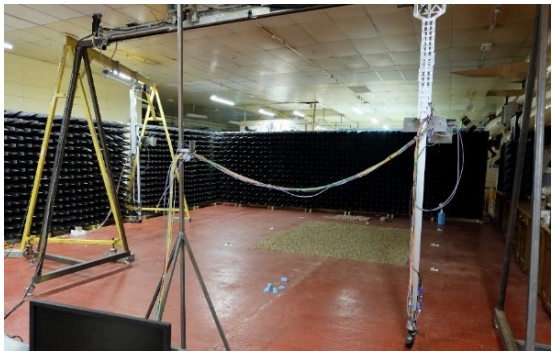

Figure 1. The GBSAR laboratory in a bistatic configuration, measuring a gravel scene.

The GBSAR laboratory performs microwave measurements with a Vector Network Analyser (VNA), which generates a stepped frequency waveform. The system was set up for indoor use, with the VNA attached to two Ultra-Wideband horn antennas allowing measurements within the range 1-10 GHz. 6.6-10 GHz was the bandwidth selected to for images in the investigation. The Antennae can be mounted in a bistatic or a pseudo monostatic configuration. When in a bistatic configuration, each antenna is mounted on a different two-dimensional vertical SAR aperture scanner. One SAR aperture is 3.5 m wide by 1.5 m high, mounted on a brown frame, and the other is 1.3 m

wide by 1.5 m high, mounted on a yellow frame, as seen in Figure 1. The measured target scene consisted of gravel, which provides a speckled SAR image suitable for the coherence investigation.

The data collection involved the transmitter antenna, mounted on the brown frame, traversing horizontally for each of nine fixed receiver antenna positions, mounted on the yellow frame.

When the scene is undisturbed, and the scans are repeated with the receiver in a new location, the combination of scans are equivalent to a single multistatic scan with multiple receivers operating simultaneously. As there are two separate trajectories for the transmitter, the GBSAR system has effectively collected two different multistatic SAR geometries. Figure 2 presents a diagram of the two multistatic scan SAR geometries. Red and green show the transmitter paths for upper and lower scan heights respectively; blue and yellow show the corresponding receiver positions when the geometry is monostatic and is partly obscured. The magenta stars show the 9 receiver positions for the various bistatic geometries collected. The black circle represents the scene centre.

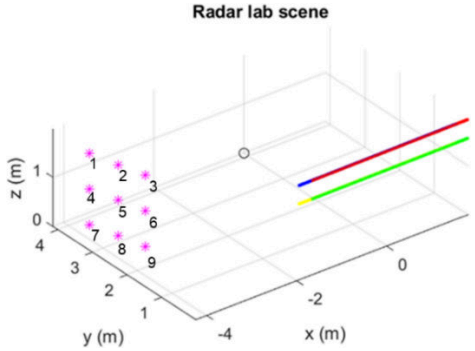

Figure 2. Monostatic and multistatic SAR geometries.

The scene used was a gravel rectangle, approximately 3.5 x 4 m, made up of approximately 1 cm sized gravel, which is around 1/3-1/5 the size of the wavelengths measured. This allowed for the appearance of speckle and would appear similar to rough flat terrain or an unsurfaced road. Had the smooth laboratory floor been left uncovered by gravel, it would have resulted in low signal to noise/clutter ratios.

In addition, the scene was disturbed between some of the multistatic collections, allowing a further validation of the CCD approach and measurements.

2.2 Spatial frequency domain

The spatial frequency domain, also called K-space, can be conceptualised in two ways. The first is as a Fourier transform of a reflectivity map of the scene, and the other as a composite of incident and scattered ray vectors with a length proportional to frequency [8].

The vector method allows the K-space image support outlines to be plotted for evaluation of SAR geometry properties, with an example shown in Figure 3.

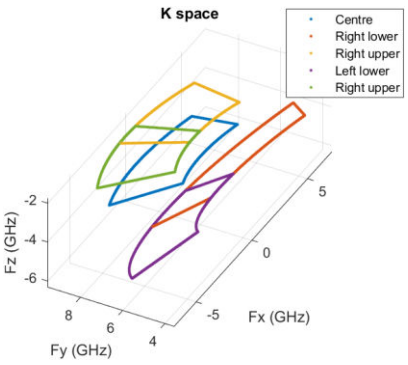

Figure 3. Image showing the Image support outlines in the spatial frequency domain, for the four corners of the gravel area and the centre (blue). This shows the large degree of radar geometry variation in the near-field SAR collection.

Data pertaining to a SAR collection can be represented in spatial frequency (K-space) as an image support. In the SAR far-field, this takes the form of a single image support [8], whereas in the more general SAR near-field case, there is an image sub-support associated with each scene position.

Here, the SAR near-field is defined as the regime where the range $d < 2L_{cr}^2 \lambda_c^{-1}$ for an image cross range extent L_{cr} and centre wavelength λ_c.

In Figure 3 the image sub-support outlines for the four corners of the scene and for the centre of the scene are presented.

Due to the SAR geometry, SAR images taken from two different radar trajectories will have different overlap when corresponding K-space sub-supports are projected vertically. For the case of a horizontal ground scene, the overlap is associated with data which is coherent between the two collections and the non-overlap is associated with incoherent energy. This association is well-known for the monostatic case [6, 8], and is investigated here for the bistatic case.

The incoherent energy can be removed from the SAR imagery, or alternatively can be excluded at the image formation step, in principle resulting in new image pairs with improved coherence between them [6, 8].

An algorithm has been developed to calculate the vertically projected K-space sub-supports for each image pixel position, and to then find corresponding overlapping and non-overlapping projected areas.

As an illustrative example, in Figure 4, vertically projected sub-supports are presented. These are associated with the image centre position, and are for three bistatic collections, where the receiver is at three different heights. Three possible collection pairings are possible, and corresponding degrees of support overlap and non-overlap indicate that some pairings will have more coherence than others.

When all image pixel positions are considered, the sum of the overlap areas and corresponding non-overlap areas can be calculated. For the specific laboratory measurement scenario, the ratio of these areas will be presented in section 4.2, for comparison with image coherence results.

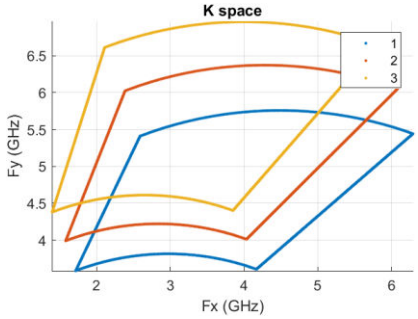

Figure 4. Vertically projected K-space sub-supports, for the scene centre, for reciever positions 1, 2 and 3 (see Figure 2).

2.3 Coherence

Coherence can be described of as the product of three main effects, described by factors in the range 0 to 1, where 0 corresponds to low coherence, and 1 corresponds to high [6, 9]. This is typically used for the far-field monostatic case; however, this paper investigates the generalisation to the near-field bistatic case.

$$\gamma = \gamma_{temp}\gamma_{SNR}\gamma_{proc} \tag{2}$$

Where, γ_{temp} refers to temporal changes within the scene, such as the movement of scatterers. These might be natural such as those caused by the rain and wind or by human interaction, such as a vehicle creating tracks. If there were no changes in the scene this value would tend to 1. If there were significant change in the scene, then the value would be close to 0. γ_{SNR} refers to losses in coherence due to noise; γ_{proc} refers to effects due to processing, and can be described as follows,

$$\gamma_{proc} = \gamma_{algorithm}\gamma_{registration}\gamma_{RCS}\gamma_{baseline} \tag{3}$$

The processing term encompasses errors arising from approximations in the SAR imaging algorithm, $\gamma_{algorithm}$, image registration errors, $\gamma_{registration}$, changes to the RCS, γ_{RCS}, and SAR geometry effects, $\gamma_{baseline}$.
The baseline factor $\gamma_{baseline}$ refers to decorrelation due to differences with the radar platform trajectories and in principle can be increased (brought closer to 1) through incoherent energy trimming (discarding) [2, 6, 8].

$$\gamma_{baseline} = \frac{A_c}{\sqrt{A_r A_m}} \tag{4}$$

Where A_c is the area of the overlap in the K-space supports. A_r and A_m are the areas for the reference and mission K-space supports respectively.
The γ value is regarded as *true* values, whereas the values obtained from the ROI in the CCD images are slightly different, in that they are measured and are a biased estimate of the true values [6, 9, 10]

3 Methodology

This paper employs simulated data and experimental data for validation. The simulation employs the laboratory ground truth and SAR geometries.
The simulation assumes perfect isotropic point scatterers and does not account for shadowing or multipath.
It was ensured that fully developed speckle was present in the images by comparing simulated images with the known position of scatterers, as seen in Figure 5, and also by verifying that the intensity distribution across the Region of Interest (ROI) conformed to the Rayleigh distribution (see Figure 6):

$$P(I) = \frac{1}{\langle I \rangle} exp\left(-\frac{I}{\langle I \rangle}\right) \tag{5}$$

Here I is the intensity and $\langle I \rangle$ is the mean intensity [8, 11].

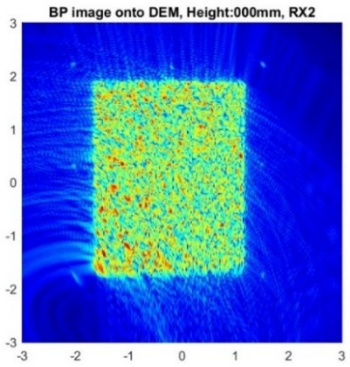

Figure 5 (a). Example simulated bistatic SAR image, with the transmitter in the upper track and reciever at position 2.

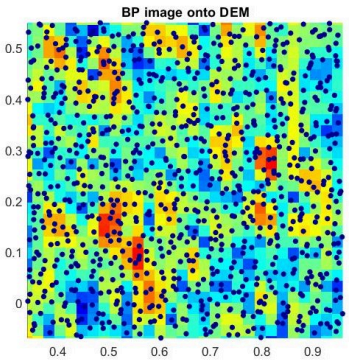

Figure 5 (b). Zoomed in view of a simulated SAR image with scatterer positions overlaid with dark blue dots.

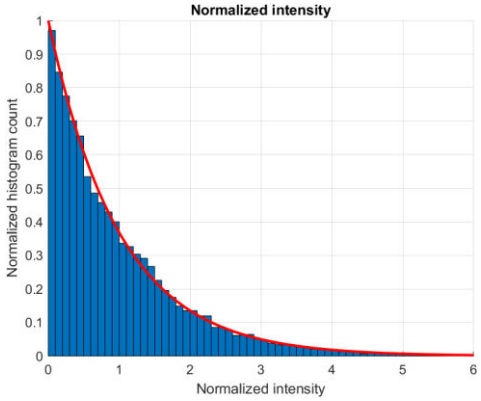

Figure 6. Histogram showing the normalised intensity of a simulated SAR image, with the Rayleigh distribution curve in red.

The CCD algorithm was then applied to find the coherence between the scans at different heights and between the geometries with different bistatic receiver positions. All coherence averaging was done over the gravel ROI only.

4 Results

After formation of monostatic and bistatic SAR images, the CCD process is applied between pairs of images, providing both CCD image results and an overall coherence value for each pair of images. The coherence values are listed in tables in sections 4.1 and 4.2.

4.1 Monostatic results

The overall coherence for the gravel covered ROI in the measured monostatic images are shown in Table 1. The table shows the mean coherence over the ROI between the different linear polarisation channels and for the two different grazing angles. The antenna scanner travels at two heights, an upper "u" and a lower "l" (1.925 m & 1.543 m) giving the grazing angles 25.1° and 20.6° to the scene centre respectively.

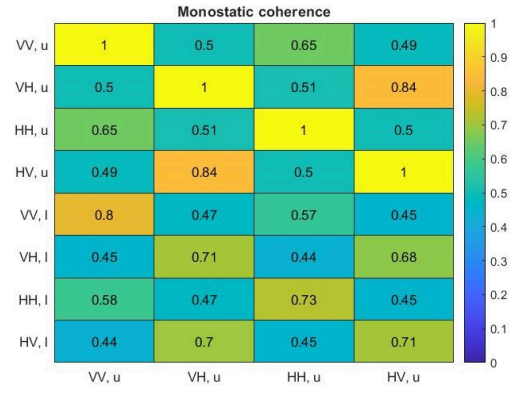

Table 1. Heat map showing the estimated mean coherence between measured monostatic image pairs in different linear polarisations. The height is shown as "u" for the upper scan position and "l" for the lower position. The coherence value is for the gravel RoI only.

Within the upper scan heights, the table is symmetric and demonstrates several patterns. Coherence between co-polarisations (HH and VV) is better than that between co-polarisations and cross-polarisations (HV and VH). The cross-polarisations correlate well with each other, (γ = 0.84), however the two channels are not identical. This could be due to the pseudo-monostatic geometry, where the transmitter and receiver horns are side-by-side, and due to the SAR near-field nature of the geometry.

Comparisons can then be made between the two heights. These are shown in Table 2. Using the radar platform trajectories, $\gamma_{baseline}$ could be calculated from the K-space overlap [6]. Then the following approximation:

$$\gamma_{RCS} \approx \gamma / \gamma_{baseline} \qquad (6)$$

was used to calculate γ_{RCS}. This approximation could be used as γ_{temp}= 1 as there was no change; $\gamma_{algorithm}$ and γ_{reg} both have values approaching 1; γ_{SNR} ≈1 using an estimated SNR of -45 dB, although this will vary across the scene. There is a significant level of clutter present from multipath and is included under γ_{RCS}, which varies with polarisation. The VV images had a greater coherence than the VH, HH and HV images when compared across the different heights within the same polarisation. With a coherence of 0.8 as opposed to 0.71-0.73. This is reflected in a corresponding higher γ_{RCS}. This may be due to H polarised waves being more susceptible to ground multipath effects [12].

Simulations resulted in an estimated coherence of 0.89 when comparing the two different monostatic geometry heights and $\gamma_{baseline}$ was evaluated as 0.93. However, in the simulation γ_{RCS} would be equal to one, hence in the simulation, it would be expected that $\gamma_{baseline} = \gamma$. It is possible that the observed small difference is due to random nature of the set scatterer distribution in the simulation or due to the pixelized approach used to find the projected area of the K-space sub-supports.

	γ	$\gamma_{baseline}$	γ_{RCS}
VV	0.8	0.93	0.86
VH	0.71	0.93	0.76
HH	0.73	0.93	0.78
HV	0.71	0.93	0.76
Average	0.74	0.93	0.79

Table 2. Table showing coherence values when comparing different monostatic heights. These were used to calculate γ_{RCS} (equation (6))

4.2 Bistatic results

The multistatic collections contained two transmitter heights and for each of these, nine bistatic SAR geometries with individual receiver positions. These were used to form bistatic pairs to perform CCD analysis on; the geometries are shown in Figure 2. The measurements were fully polarimetric, with all four linear polarisations collected.

For each generated CCD image, an average coherence value over the ROI was generated. For each pair of SAR geometries, the mean value of the coherence across the four

polarisations was found. This mean was then subtracted from the coherence values for the different polarisations.
The histogram in Figure 7 shows the distribution of coherence minus mean across the four polarisations, for all SAR geometry pairs.

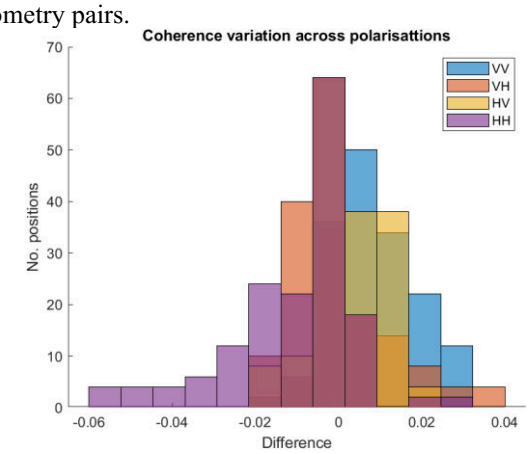

Figure 7. Histogram showing the distribution of variation from the mean coherence for each SAR geometry pair, across the four polarisations.

Figure 7 shows that despite having a very low standard deviation, the effect of RCS is still significant. $\gamma_{baseline}$ is still the dominant factor as it resulted in the coherence varying from 0.3-1, when looking at different receiver positions within any given polarimetric channel, as seen in Table 3. Whilst the average standard deviation may only have been around 1% of the maximum coherence, Figure 7 shows that HH tends to have a below average coherence, with VV having a higher than average. VH and HV where both close to the mean.
It is noted that the scene was relatively homogenous, consisting only of gravel and it is likely that more complex targets could result in a greater degree of difference in γ_{RCS}.

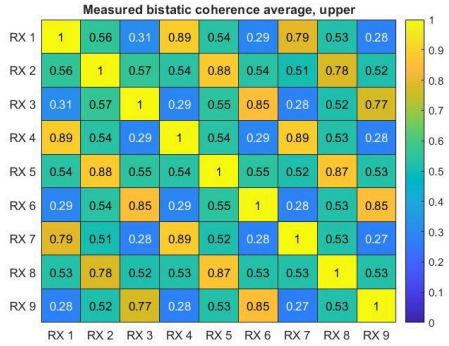

Table 3. Table showing the coherence between the measured nine receiver position bistatic SAR images collected with the transmitter in the upper position, averaged across polarisations.

In Table 3, a pattern emerges where, noting that the receiver positions are in a 3 X 3 square grid (see Figure 2) the grid receiver columns have a good coherence of 1-0.8. A step away in the receiver row direction for an image pair lowers the coherence to 0.5-0.6, and a second step away lowers it to around 0.3.
Table 4 presents the *simulated* SAR image coherence results. These results do not only exhibit the same pattern as for the measured data, but their values also align very closely with the measured polarisation averaged coherence.

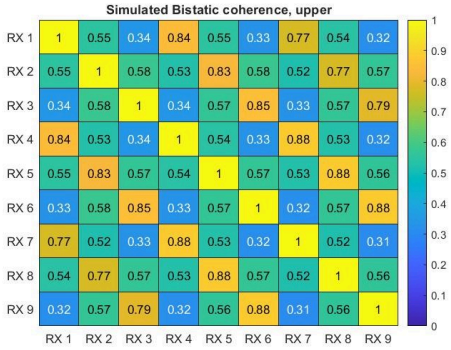

Table 4. Table showing the coherence between the simulated nine receiver position bistatic SAR images, with the transmitter in the upper position.

The difference between the measured coherence values (averaged across polarisations) and the simulated coherence values can be calculated. For both the upper and lower tracks. A histogram of these difference values is shown in Figure 8.

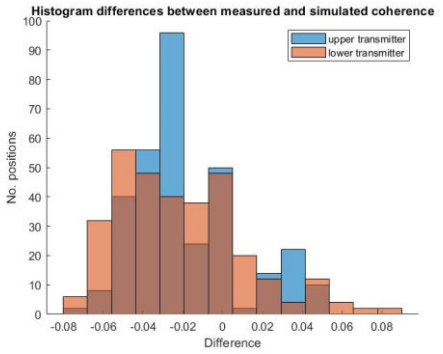

Figure 8. Histogram of the differences between the measured polarisation averaged coherence results in Table 3 and the simulated coherence results in Table 4. The mean difference value is -0.03.

With the knowledge of the SAR geometries, the K-space projected sub-support overlap values can be used to calculate $\gamma_{baseline}$ as shown in equation (4). The $\gamma_{baseline}$ values are shown in Table 5. These are evaluated for the ROI only. As discussed in section 2.2, because the collections are in the SAR near-field regime, the calculation is performed for every scene position, or pixel, so that the overlap across the whole ROI may then be estimated.

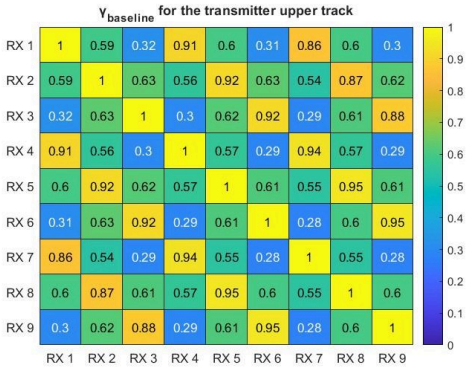

Table 5. Table showing $\gamma_{baseline}$ values for the upper transmitter trajectory. These were calculated for each pixel and then averaged across the ROI.

The measured coherence values can also be used to estimate the γ_{RCS} using equation (6). This then allows the γ_{RCS} values to be plotted on a histogram. These values then had the mean γ_{RCS} for each bistatic geometry pair subtracted, to show a distribution (in a similar manner to Figure 7).

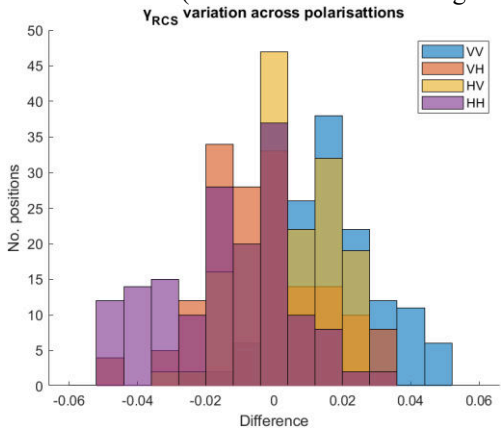

Figure 9 Histogram showing the distribution of γ_{RCS} from the mean γ_{RCS} for each SAR geometry pair, across the four polarisations.

Estimation of γ_{RCS} shows that it varies depending on polarisation. For this particular scene the HH tends to result in a lower value and the VV tend to be higher. This reflects the pattern in Figure 7.

5 Conclusion

The monostatic and bistatic results demonstrate that the proportion of coherence due to the SAR geometry is a dominating factor in these laboratory experiments. This can be seen in the similarity between the measured data coherence and $\gamma_{baseline}$, which acts as an upper bound on the true coherence.

It's noted that the measured coherence was very similar to the simulated coherence, despite the simplicity of the simulation, which relied upon isotropic point scatterers.

However $\gamma_{baseline}$ cannot be thought of as the only factor with a significant impact. γ_{RCS} still effects the coherence, even when the radar platform trajectories were very similar, and targets very simple. This was shown in Figure 7 and Figure 9. It is also likely that a more complex terrain, where the RCS varies significantly depending on the viewing angle, could lead to this component being more significant. The value of γ_{RCS} varied between polarisations and positions, this is not only due to the varying RCS of the gravel but also may have been due to the laboratory clutter and layout, leading to multipath echoes. Multipath is stronger in some polarisations as opposed to others [12]. It is possible that a fully polarimetric collection may offer improved coherence overall, using polarimetric decompositions or polarimetric CCD algorithms, as this could reduce the overall impact of γ_{RCS} in reducing coherence.

Overall, the results show that the equations for coherence found in [6, 9] (equations (2) and (3)) do apply to the bistatic case.

Future work could focus on comparing across polarisations and polarimetric decompositions. Additionally using multistatic images, as opposed to individual bistatic images from a multistatic collection, which could provide finer resolution SAR images. Additionally, more complex terrain with varying RCS could be investigated.

6 Literature

[1] R. Bamler and P. Hartl, "Synthetic aperture radar interferometry," *Inverse Problems*, vol. 14, no. 4, 1998, doi: 10.1088/0266-5611/14/4/001.

[2] D. Andre, "Bistatic SAR coherence improvement through spatially variant polarimetry," 2015.

[3] D. Andre, K. Morrison, D. Blacknell, D. Muff, M. Nottingham, and C. Stevenson, "Very High Resolution Coherent Change Detection," 2015.

[4] D. Andre, D. Blacknell, and K. Morrison, "Spatially variant incoherence trimming for improved SAR CCD," 2013.

[5] E. Kulu, "Small Launchers-2021 Industry Survey and Market Analysis," Kepler Communications, 2021. [Online]. Available: www.newspace.im

[6] M. Preiss and J. Stacy, "Coherent Change Detection: Theoretical Description and Experimental Results," 2006.

[7] C. López-Martínez and E. Pottier, "Basic Principles of SAR Polarimetry," in *Remote Sensing and Digital Image Processing*, vol. 25, Springer Science and Business Media B.V., 2021, pp. 1–58. doi: 10.1007/978-3-030-56504-6_1.

[8] C. v. Jakowatz, D. E. Wahl, P. H. Eichel, D. C. Ghiglia, and P. A. Thompson, *Spotlight-mode synthetic aperture radar a signal processing approach*. Kluwer Academic Publishers, 1996.

[9] H. A. Zebker, S. Member, and J. Villasenor, "Decorrelation in Interferometric Radar Echoes," 1992.

[10] A. J. Bennett, D. Blacknell, K. Martin, and D. B. André, "Prediction of coherent change detection performance in SAR," in *Algorithms for Synthetic Aperture Radar Imagery XVIII*, May 2011, vol. 8051, p. 80510Z. doi: 10.1117/12.883833.

[11] Andre D, Morrison K, Blacknell D, Muff D, Nottingham M, and Stevenson C, "Very High Resolution SAR Speckle and CCD," 2015.

[12] E. Knott, J. Shaeffer, and M. Tuley, *RADAR cross section*, 2nd ed. Artech House, 1993.

Polarimetric bistatic SAR image coherence

Hagelberg, Alexander

2022-11-10

Hagelberg A, Andre D, Finnis M. (2022) Polarimetric bistatic SAR image coherence. In: EUSAR 2022: 14th European Conference on Synthetic Aperture Radar, 25-27 July 2022, Leipzig, Germany
https://ieeexplore.ieee.org/document/9944219